Article

Cation-Size Mismatch as a Design Principle for Enhancing the Efficiency of Garnet Phosphors

Yoon Hwa Kim,[⊥] Ha Jun Kim,[⊥] Shyue Ping Ong, Zhenbin Wang,* and Won Bin Im*

Read Online

ACCESS | Metrics & More | Article Recommendations | SI Supporting Information

ABSTRACT: In this study, we report on the development of a new garnet phosphor with enhanced optical properties and cost reduction. Samples were prepared using the solid-solution method, in which the chemical unit and substitutions with cation-size mismatch were combined. Solid solutions between two garnet structure compounds, green phosphor $Lu_3Al_5O_{12}:Ce^{3+}$ (LuAG:Ce^{3+}) and orange phosphor $Lu_2CaMg_2Si_3O_{12}:Ce^{3+}$ ($Lu_{3-x}Ca_xAl_{2-2x}Mg_{2x}Al_{3-3x}Si_{3x}O_{12}:Ce^{3+}$), constituted the complete solid-solution range x ($x = 0-1$). The crystal structures of all the compounds were discerned through Rietveld refinement based on the X-ray diffraction patterns. The unique occupancy of {Lu/Ca}, [Al/Mg], (Al/Si), and O atoms in the solid-solution samples was identified. Optical properties were classified in terms of the excitation and emission spectra, quantum yield, and temperature-dependent photoluminescence intensity. To investigate the relationship between the structural and optical changes, Ba^{2+} ions (employed for cation-size mismatch) were substituted into dodecahedral and octahedral sites at various concentrations. Finally, we report the development of a new green garnet phosphor via the use of a solid-solution design and cation-size mismatch, the emission intensity of which was measured 116% higher than that of commercial LuAG:Ce^{3+}.
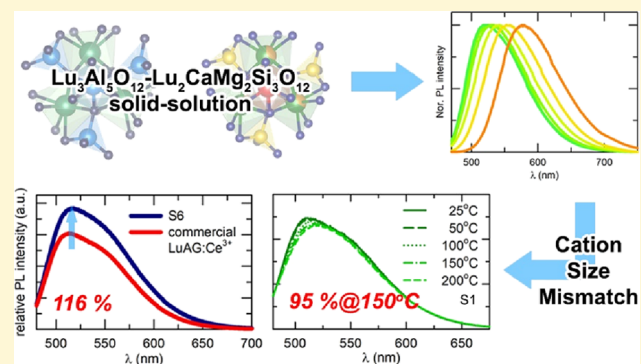
1. INTRODUCTION

Since the development of phosphor-converted white light-emitting diodes (pc-WLEDs) combined with blue InGaN LEDs and yellow $Y_3Al_5O_{12}:Ce^{3+}$ (YAG:Ce^{3+}) garnet phosphors, Ce^{3+}-doped garnet phosphors have been widely investigated because of their high thermal stability, efficiency, and color-tunable emissions. The general structure of garnet is ${A}_3[B]_2(C)_3O_{12}$, forming a body-centered cubic unit cell of the $Ia\bar{3}d$ space group (#230) with cations in special positions (24c, 16a, and 24d sites) and oxygen anions in general positions (96h site). The three cations have different coordinations that are shared with the oxygen ions: the {A} cations are dodecahedral with eight coordination, the [B] cations inhabit the octahedral sites, and the (C) cations are in the tetrahedral sites.[1] The emission spectra of garnet phosphors can be controlled by varying the crystal-field splitting (ε_{cfs}) and the nephelauxetic effects of Ce^{3+} ions. For example, the YAG:Ce^{3+} phosphor, which is a representative garnet phosphor used in lighting applications, emits yellow light ($\lambda_{em} = \sim540$ nm) under blue excitation ($\lambda_{ex} = 450-470$ nm) because of the large ε_{cfs} of the Ce^{3+} ions within the structure. These excitation and emission processes result from electronic transitions that occur between the $[Xe]4f^1 5d^0 6s^0$ ($^2F_{5/2}, ^2F_{7/2}$) and $[Xe]4f^0 5d^1 6s^0$ ($^2D_{3/2}$) states within the Ce^{3+} ions. The position of the Ce^{3+} 5d levels is strongly influenced by the selection of a host lattice, and Ce^{3+} emissions can

therefore be controlled via the careful substitution of cations in the dodecahedral, octahedral, and tetrahedral sites. The choice of cations allows the modulation of the local environment of the Ce^{3+} ions and thus the important properties of the centroid shift (ε_c) and ε_{cfs}, which are connected to the optical properties. The color emitted by Ce^{3+}-doped garnet phosphors can be changed from green to yellow and even orange-red via the substitution of various cations.

The solid-solution method is practical for developing new optical properties using isomorphism and/or pseudo−isomorphic relationships and by varying the local crystal field strength around the activators.[2] Many research groups have focused on the solid-solution design of garnet structures via cationic or anionic substitution in order to tune the optical properties of existing phosphors and to find new phosphors. New structural and optical properties have been reported from substitutions carried out at various sites (dodecahedral, octahedral, and tetrahedral) in the structure of garnet using

this method. One option is substitution into one cation site, such as substituting Lu^{3+} ions into the dodecahedral site of the YAG:Ce^{3+} phosphor[3] or Ga^{3+} ions into the tetrahedral site of the $Y_3Sc_2Al_3O_{12}$:Ce^{3+} phosphor; another is the substitution into two cation sites with charge compensation, such as substituting the Al^{3+} ions in the octahedral and tetrahedral sites of YAG:Ce^{3+} with Ga^{3+} ions by increasing the concentration of Ga^{3+} ions or substituting Mg^{2+} ions into the octahedral site and Si^{4+}/Ge^{4+} ions into the tetrahedral site of the YAG:Ce^{3+} or $Lu_3Al_5O_{12}$:Ce^{3+} (LuAG:Ce^{3+}) phosphors, or into the $\{Ca\}_3[Sc]_2(Si)_3O_{12}$-$\{Lu_2Ca\}[Mg]_2(Si)_3O_{12}$:$Ce^{3+}$ solid-solution phosphor. Finally, all the cation sites in the garnet structure can be replaced, together with the $\{Ca^{2+}\}$-$[Mg^{2+}]$-(Si^{4+}) clusters in the LuAG:Ce^{3+} phosphor.[3−10] However, considerable challenges remain in the evolution of structural and optical properties of solid-solution garnets *via* multiple substitutions.

A cation-size mismatch that changes the average ionic radius $\langle r \rangle$ can also occur, thereby changing the strain in the lattice.[11] The cation-size variance (σ^2) describes the size distribution that varies quadratically with the molar ratio x. Previous studies in which the σ^2 was held constant in a series of ferromagnetic, superconductor, and ferroelectric materials indicated that the respective magnetic Curie, superconducting critical, and ferroelectric Curie transition temperatures all had strong linear correlations with the electronic transitions and σ^2.[12,13] This concept has also been applied for increasing the quantum efficiency of $M_{1.95}Si_{5-x}Al_xN_{8-x}O_x$:$Eu^{2+}$ and $Sr_{1.98-x}(Ca_{0.55}Ba_{0.45})_xSi_5N_8$:$Eu^{2+}$ phosphors.[14,15]

The green $Lu_3Al_5O_{12}$:Ce^{3+} (LuAG:Ce^{3+}) phosphor has the same structure ($Ia\overline{3}d$) as the YAG:Ce^{3+} phosphor, which could be used to solve the problem of the lower color-rendering index associated with the YAG:Ce^{3+} phosphor. However, the LuAG:Ce^{3+} phosphor is problematic in terms of cost because of the expense of lutetium. This study, therefore, focused on enhancing the luminescence of a LuAG:Ce^{3+} phosphor while further reducing the cost by decreasing the amount of lutetium used in the incorporation of $\{D^{2+}\}$-$[D^{2+}]$-(Si^{4+}) ion pairs into the host lattice in order to substitute the $\{Lu^{3+}\}$-$[Al^{3+}]$-(Al^{3+}) sites (D^{2+} ions = divalent ions Mg, Ca, and Ba). An in-depth and detailed investigation into the influence of these substitutions on the photoluminescence properties was conducted. It was interesting to discover that during the development of a new green garnet phosphor *via* a solid-solution design with a cation-size mismatch, the emission intensity and thermal stability were improved compared to the mother samples. The corresponding luminescence mechanisms are also discussed in detail.

2. EXPERIMENTAL SECTION

2.1. Materials and Synthesis. Powder samples with the general formula $Lu_{2.9-x}Ce_{0.1}Ca_xAl_{2-2x}Mg_{2x}Al_{3-3x}Si_{3x}O_{12}$ (LCAMAS:Ce^{3+}) (x = 0, 0.1, 0.3, 0.5, 0.7, and 1) were prepared *via* solid-state reaction from the starting materials Lu_2O_3 (Samchun, 98%), $CaCO_3$ (Aldrich, 99.99%), Al_2O_3 (Kojundo, 99.99%), MgO (Kojundo, 99.9%), SiO_2 (Kojundo, 99.99%), and CeO_2 (Kojundo, 99.999%). The concentration of cerium was optimized at 0.1 mol in the formula unit. Cation-size mismatch samples (S1−7) with the formula $Lu_{2.9-y}Ce_{0.1}D_yAl_{2-2y}D_{2y}Al_{3-3y}Si_{3y}O_{12}$ (D = Mg, Ca, and Ba, y = 0.1 and 0.3) were prepared using a method similar to that used for the production of $BaCO_3$ (Kojundo, 99.9%). The powder reagents were ground together and heated at 1450−1600 °C in a reducing atmosphere of H_2/N_2 (5%/95%) for 4 h. The samples were cooled

to room temperature after the completion of the heat treatment process. (S1: $Lu_{2.8}Ba_{0.1}Ce_{0.1}Al_{1.8}Ba_{0.2}Al_{2.7}Si_{0.3}O_{12}$,

S2: $Lu_{2.8}Ba_{0.1}Ce_{0.1}Al_{1.8}Mg_{0.2}Al_{2.7}Si_{0.3}O_{12}$,
S3: $Lu_{2.6}Ba_{0.3}Ce_{0.1}Al_{1.4}Ba_{0.6}Al_{2.7}Si_{0.3}O_{12}$,
S4: $Lu_{2.6}Ba_{0.3}Ce_{0.1}Al_{1.8}Mg_{0.2}Al_{2.7}Si_{0.3}O_{12}$,
S5: $Lu_{2.6}Ba_{0.3}Ce_{0.1}Al_{1.4}Mg_{0.6}Al_{2.7}Si_{0.3}O_{12}$,
S6: $Lu_{2.8}Ca0_{.1}Ce_{0.1}Al_{1.8}Ba_{0.2}Al_{2.7}Si_{0.3}O_{12}$, and
S7: $Lu_{2.6}Ca0_{.3}Ce_{0.1}Al_{1.4}Ba_{0.6}Al_{2.7}Si_{0.3}O_{12}$).

2.2. Characterization. The structural information about the synthesized samples was examined with the GSAS software suite using the X-ray diffraction (XRD) pattern. The XRD data were obtained using CuKα radiation (Philips X'Pert) over the angle range of 10° ≤ 2θ ≤ 120° with a step size of 0.026°. VESTA was used to draw the structure.[16] The room-temperature PL spectra were measured using a Hitachi F-4500 fluorescence spectrophotometer over the wavelength range of 300−700 nm. The quantum yield was measured at 450 nm excitation using a 150 W xenon laser (Hamamatsu C9920-02) at the Korea Photonics Technology Institute (KOPTI). The thermal quenching characteristics were measured at temperatures in the range 25−200 °C, by utilizing the integrated heater, temperature controller, and thermal sensor that are connected to the Hitachi F-4500 fluorescence spectrometer. The ^{27}Al solid-state nuclear magnetic resonance (NMR) was measured using 400 MHz NMR spectroscopy (Agilent 400 MHz 54 mm NMR DD2) at the KAIST Analysis Center for Research Advancement (KARA) in the Korea Advanced Institute of Science and Technology (KAIST). The X-ray photoelectron spectroscopy spectra were obtained using a Thermo VG Scientific instrument (Multilab 2000).

2.3. Computational Methodology. All density functional theory calculations were carried out using the Vienna ab initio simulation package (VASP) with the projector augmented wave (PAW) method.[17,18] The Perdew Burke−Ernzerhof (PBE) generalized-gradient approximation (GGA) was used to describe the exchange−correlation interactions. The plane-wave energy cutoff was 520 eV. The electronic energy and atomic force were converged within 10^{-5} and 0.01 eV/Å, respectively. The Brillouin zone was sampled with a k-point grid density of 100 by the reciprocal volume. All crystal structure manipulations and data analyses were conducted using the Python Materials Genomics (pymatgen) package.[19] The band gaps of the host materials were calculated using the PBE functional as well as the more accurate screened hybrid Heyd−Scuseria−Ernzerhof (HSE) functional.[20,21] The Debye temperatures were computed using the quasi-harmonic model. For the evaluation of the elastic tensor, the structure was first optimized with more stringent electronic energy and atomic force tolerances of 10^{-7} eV and 10^{-3} eV/Å, respectively. The elastic tensor was then computed with an electronic energy convergence criterion of 10^{-7} eV, and the elastic moduli were calculated using the Voigt−Reuss−Hill approximation.[22,23]

3. RESULTS AND DISCUSSION

3.1. Changes to the Structural and Optical Details in the Solid Solution of Garnet Phosphors. The structural analysis of the synthesized compounds indicated that the $Lu_3Al_5O_{12}$−$Lu_2CaMg_2Si_3O_{12}$ (LuAG−LCMS) solid-solution garnet synthesized at an ambient pressure tends to favor compositions with larger cations, such as Ca^{2+} ions, which partially occupy the {A} dodecahedral site. Larger ions, such as Mg^{2+} at [B] octahedral sites, and smaller ions, such as Si^{4+} at (C) tetrahedral sites, also help to stabilize the formation of the garnet phase. This interplay between the substituent ions and their occupancy within the garnet plays a role in the stability and phase purity of the garnets. Therefore, compositions were constructed in which Ca^{2+} ions were substituted for the Lu^{3+} ions in the dodecahedral sites, Mg^{2+} ions were substituted for the Al^{3+} ions in the octahedral sites, and Si^{4+} ions were substituted for the Al^{3+} ions in the tetrahedral sites, with charge compensation.
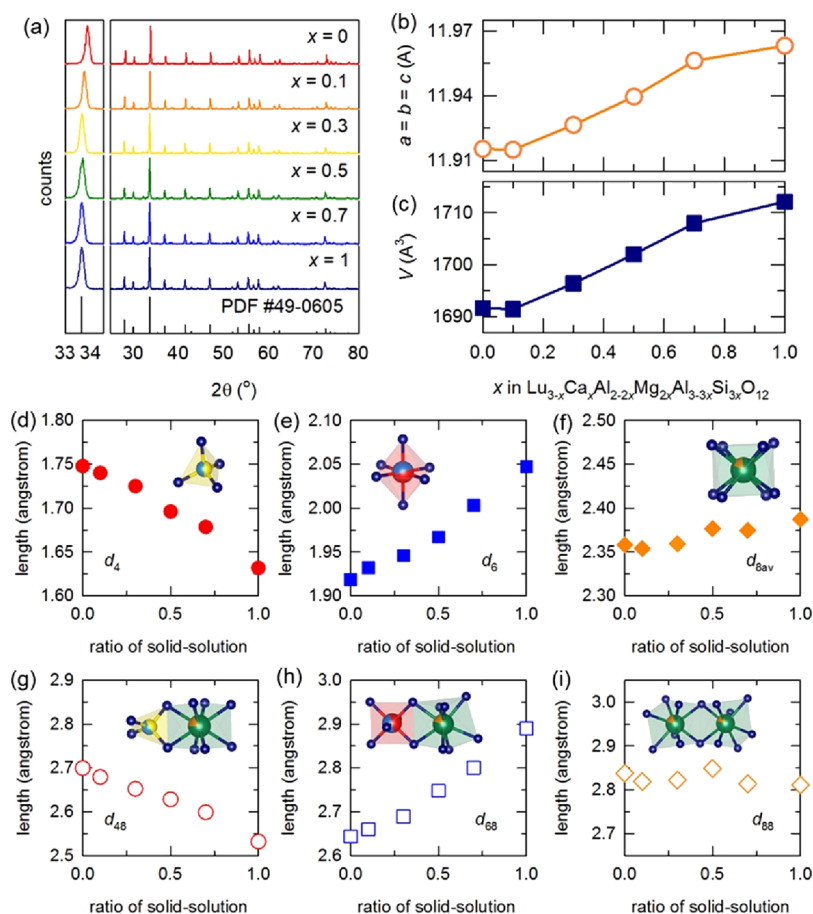
Figure 1. (a) (left) Magnified and (right) XRD patterns of $Lu_{3-x}Ca_xAl_{2-2x}Mg_{2x}Al_{3-3x}Si_{3x}O_{12}$:$Ce^{3+}$ acquired at room temperature for x, as indicated. Evolution of the (b) lattice parameter and (c) volume from Rietveld refinement as a function of the solid-solution ratio, x. (d−f) The mean cation−oxygen interatomic distance plotted against the solid-solution ratio, x. (d), (e), and (f) are shown as the variation of d_4, d_6, and d_{8av} against the solid-solution ratio (x), respectively. (g−i) Mean oxygen−oxygen interatomic distance plotted against the solid-solution ratio, x. (g), (h), and (i) are shown as the variation of d_{48}, d_{68}, and d_{88} against the solid-solution ratio (x), respectively. Polyhedra are shown in the inset figure, with arrows denoting the corresponding length in the structure for the (Al,Si)−O tetrahedra, [Al,Mg]-O octahedra, and {Lu,Ca}-O dodecahedra.

Figure 1a presents the results of the XRD patterns of the LuAG-LCMS solid-solution series (x = 0, 0.1, 0.3, 0.5, 0.7, and 1). The starting model was built with crystallographic data taken from JCPDS PDF #49-0605 LuAG. The linear shifts in the lattice parameters of the series, represented by the increasing x, are plotted in Figure 1b,c. The parameters of the lattice of the solid-solution garnet phosphors were found to increase in all compositions, where the Ca^{2+} ions nominally replaced the Lu^{3+} ions in the dodecahedral sites, Mg^{2+} ions replaced the Al^{3+} ions in the octahedral sites, and Si^{2+} ions replaced the Al^{3+} ions in the tetrahedral sites. This increase in the lattice parameter was expected as larger cations Ca^{2+} (r_{CaO_8} = 1.26 Å) and Mg^{2+} (r_{MgO_6} = 0.86 Å) were used to replace the smaller cations Lu^{3+} (r_{LuO_8} = 1.12 Å) and Al^{3+} (r_{AlO_6} = 0.62 Å) on the dodecahedral and octahedral sites, respectively.

Another substitution that was carried out on the tetrahedral site was the replacement of Al^{3+} (r_{AlO_4} = 0.53 Å) with Si^{4+} (r_{SiO_4} = 0.40 Å), where the replacement of a smaller cation with a larger one counterbalanced the changes in the size of the lattice.[24] However, the overall trend was generally an increase in the size of the unit cell. The increase in the lattice parameter with the substitution of {Lu^{3+}}-[Al^{3+}]-(Al^{3+}) with {Ca^{2+}}-[Mg^{2+}]-(Si^{4+}) in LuAG is clearly seen in the LCAMAS:Ce^{3+} compositions throughout the entire range from LuAG (a =

11.92 Å) to LCMS (a = 11.96 Å), with the lattice parameters of the end-member compositions in reasonable agreement with results attained in previous studies.[8,25] This confirms that the lattice parameters of the solid solution in the garnet structure deviate from Vegard's law, as reported by Nakatsuka et al.[1] Tables S1 and S2 present the detailed structural parameters of the LCAMAS:Ce^{3+} compositions. The values of R_p and R_{wp} in Table S1 were used to estimate the reliability of the refinement results. The garnet structure has many edges that are shared between adjacent polyhedrons. The tetrahedron and octahedron share edges with two and six triangular dodecahedra, respectively. The triangular dodecahedron shares edges with two tetrahedra, four octahedra, and four other triangular dodecahedra, respectively, as shown in the inset of Figure S1a,b. The tetrahedra and octahedra are linked by the sharing of their corners. It is particularly relevant that the octahedron shares edges with the oxygen at the top (or bottom) of the dodecahedrons, and the tetrahedron shares edges with the oxygen at the same height as the dodecahedron.

Figure 1d−f show the variation in the cation−oxygen distances of the tetrahedra, octahedra, and dodecahedra with the variation in the composition (x), respectively. The interatomic distances d_i (i = 4, 6, 8, 48, 68, 88) are labeled in the inset of the corresponding figures. As x is increased from 0 to 1, the bond length of the tetrahedron (d_4) decreases (Δd_4

≈ 0.116 Å) while the bond length in the octahedron (d_6) increases ($\Delta d_6 \approx 0.129$ Å). This variation in cation−oxygen distances is a result of the displacement of oxygen anions that is caused by the substitution of the smaller Si^{4+} ions in the (Al^{3+}) tetrahedral site and the larger Mg^{2+} ions in the [Al^{3+}] octahedral site. This can therefore be interpreted as a movement of O atoms from the four-coordinated sites due to the contraction of the tetrahedron and the expansion of the octahedron. It is apparent from Figure 1f that this causes some of the cation−oxygen bonds to contract and some to expand, although the average bond length d_{8av} ($\Delta d_{8av} \approx 0.029$ Å) from one end member to the next is slightly elongated. Figure 1g−i show the variation in the oxygen−oxygen distance with the shared dodecahedra, tetrahedra, and octahedra and the variation in the composition (x), respectively.

The bond lengths of the edges shared with the tetrahedron and dodecahedrons (d_{48}) and the octahedron and dodecahedrons (d_{68}) change drastically, while the bond length of the edge shared with the other dodecahedrons (d_{88}) does not change significantly. In LuAG ($x = 0$), d_{48} is longer than d_{68}. However, on forming a solid solution with LCMS, this is inverted for values of x that are larger than 0.3 when d_{48} is shorter than d_{68}. The value of d_{88} does not generally follow a regular trend, although it decreases from along the compositional line. Nakatsuka et al.[1] reported that such changes in the interionic distance among anions with shared edges has a serious effect on the shielding of the anions forming the polyhedra. The analysis of these shared edges suggests that the repulsive force between the cations in the dodecahedra and the tetrahedra across d_{48} decreases when x is increased and that those in the dodecahedra and octahedra across d_{68} simultaneously increase. The interaction between the cations across the shared edge d_{88} of the adjacent dodecahedra varies from composition to composition and follows a sinusoidal pattern along the compositional line, while being generally lower for LCAMAS:Ce^{3+} ($x = 1$). The extent of the interaction between the cations should be influenced not only by the decrease in the shielding effect but also by the enhancement of the ionicity of the cation−oxygen bonds. The results in Figure 1g−i imply that the shielding effect of the anions that form the polyhedral shared edges, which relax the repulsive force between the cations in the dodecahedra and the tetrahedra and octahedra sites with increasing x, is counterproductive. The cation−cation repulsive force across the shared edges will decrease in the tetrahedra and increase in the octahedra as the content of x increases. The proportion of covalent bonding in the cation−oxygen bonds can be estimated from the bond strength; the results indicate that the covalency of the [Mg^{2+}]−O bond is greater than that of the [Al^{3+}]−O bond at the octahedral site.

As mentioned above, the octahedron shares edges where oxygen is at the top (or bottom) of the dodecahedron, and d_{68} ($\Delta d_{68} \approx 0.246$ Å) increases as x increases. This is accompanied by an increase in the angle O_{oct}-{Lu/Ca}-O_{oct}, from approximately 68.15° to 74.47°. The tetrahedron shares edges with the oxygen in the height of the dodecahedron, and d_{48} ($\Delta d_{48} \approx 0.168$ Å) decreases with the increase in x. This causes the angle O_{tet}-{Lu/Ca}-O_{tet} to decrease from approximately 71.69° to 65.68°.

The color of the body of LuAG:Ce^{3+} was green, with an emission maximum at approximately 526 nm ($\lambda_{ex} = 450$ nm) due to the highest energy Ce^{3+} 4f → 5d absorption in the blue spectral region. In the LCAMAS:Ce^{3+} compositions, the lowest

energy Ce^{3+} 4f → 5d absorption is at lower energies with a larger value of x, thereby producing a yellow-orange body color. The photoluminescence excitation spectra of the solid-solution compound series are shown in Figure 2a. There are
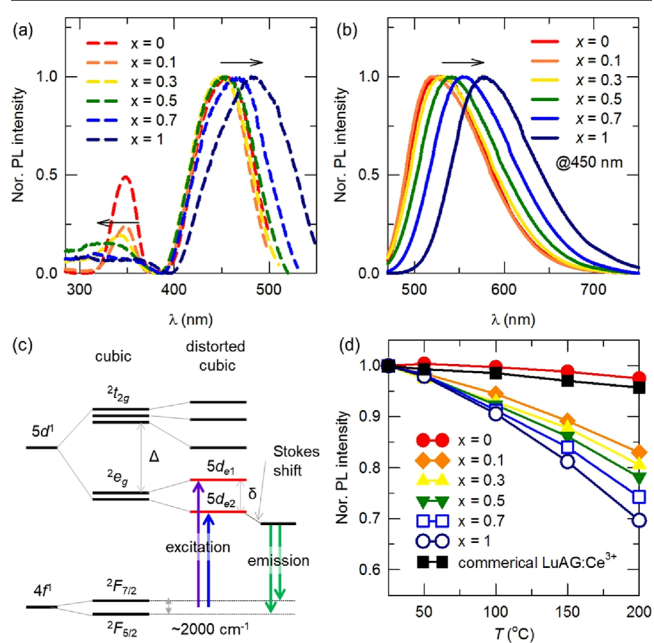
Figure 2. (a) Excitation and (b) emission spectra of $Lu_{3−x}Ca_xAl_{2−2x}Mg_{2x}Al_{3−3x}Si_{3x}O_{12}$:$Ce^{3+}$ for x, as indicated. (c) Approximated energy diagram showing the lowest energy ground-state component and the first excited 5d state of Ce^{3+} in garnets. The cubic crystal field splitting is indicated by Δ and noncubic splitting by δ. (d) Temperature dependence of normalized emission intensities ($\lambda_{ex} = 450$ nm) of the solid-solution ratio (x) and commercial $Lu_3Al_5O_{12}$:Ce^{3+} green phosphor.

two major excitation bands that originate from the transitions in the ground state and two crystal field split 5d excited states ($5d_{e1}$ and $5d_{e2}$). The peak excitation of high energy ($5d_{e1}$, low wavelength) is shifted slightly toward the higher energy region up to LCAMAS:Ce^{3+} ($x = 0.3$), after which it shifts to the higher energy region with a broadening of the spectrum. These shifts were accompanied with a reduction in the intensity, and the band ceased to exist on reaching LCMS:Ce^{3+} ($x = 1$). This indicates that the $5d_{e1}$ level shifts closer to the conduction band and loses electrons through thermal excitation. The excitation peak in the low-energy region ($5d_{e2}$) shifts progressively toward the high wavelength after LCAMAS:Ce^{3+} ($x = 0.5$). Figure 2b shows the emission spectra of the compounds on excitation with 450 nm radiation. The emission spectra shifted progressively toward the lower energy (red-shift) region of the spectra on increasing the value of x. The emission maxima in this series is influenced by the lattice structure and is shifted to a region of longer wavelength with x because of the sensitivity of the Ce^{3+} 5d levels to the surrounding electronic environment. The Ce^{3+} emission color can be tuned from green to orange by systematically replacing {Lu^{3+}} with {Ca^{2+}}, [Al^{3+}] with [Mg^{2+}], and (Al^{3+}) with (Si^{4+}). The Ce^{3+} emission bands are broadened by the spin−orbit splitting of the $4f^1$ ground state. The emission spectrum can be deconvoluted into two Gaussians separated by approximately 2000 cm^{-1} in all compositions. This is typical for the Ce^{3+} 5d → 4f emission and is indicative of emission from the lowest

energy 5d level to the $^2F_{5/2}$ and $^2F_{7/2}$ levels. The maximum wavelength of the emission (λ_{em}), the full-width-at-half-maximum (fwhm) of the emission spectra, the adsorption efficiencies, and quantum yield (QY) results that were measured at room temperature for the solid-solution ratio (x) are summarized in Table S3. The λ_{em} is red shifted, moving from the green (526 nm) to the orange (578 nm) region, and the fwhm increases with the increase in x. These results mean that the coordination environments around the Ce^{3+} ions changed continuously, leading to a red-shift in the emission (decreased energy) and a broadening of the fwhm. The adsorption efficiencies and QY values mean that these phosphors can be applied in lighting applications, such as phosphor-in-glass for headlamps or backlighting for displays, among others. Figure 2c shows a schematic energy-level diagram for Ce^{3+} in garnet. It is evident that the emission wavelength depends on both the overall 4f−5d separation and ε_{cfs} of the 5d levels. Within a single group of materials, such as garnets, the 4f−5d separation is approximately constant so that the crystal field effect dominates. The distorted cubic site occupied by Ce^{3+} is strongly compressed along one axis, resulting in an approximately tetragonal field at the lanthanide site. The extent of the tetragonal distortion at the lanthanide site affects the energy of the Ce^{3+} absorption and the emissions from the garnet. Increasing the compression on the cube increases the energy difference between the two lowest lying d-states, δ, and shifts the lower excited state energy level ($5d_{e2}$; $d_{x_2-y_2}$ orbital) to even lower energies, while shifting the second lowest excited state level ($5d_{e1}$; d_{z_2} orbital) to higher energies. The excitation and emission spectra, the values of δ, the Stokes shift, and the average electronegativity (χ_{av}) are given in Table 1.

Table 1. Spectroscopic Properties and Average Electronegativity of the Solid-Solution Phosphor Depending on the Ratio (x), Recorded at Room temperature

host composition (x)	λ_{ex1} (nm)	λ_{ex2} (nm)	δ^a (cm^{-1})	Stokes shift^b (cm^{-1})	average electronegativity (χ_{av})
0	349	456	6723.48	2918.41	1.48
0.1	346	456	6971.91	2735.97	1.49
0.3	343	451	6981.57	3305.02	1.51
0.5	329	453	8320.08	3590.77	1.52
0.7	317	467	9934.68	3330.09	1.54
1	305	481	11996.86	3488.98	1.57

$^a\delta$ is the energy difference between the two lowest lying d-states of the samples, calculated as the difference between the maxima of the excitation bands at room temperature. ^{b}The Stokes shift calculated as the difference between the maxima of the excitation band and the first emission, derived from the measurements at room temperature.

The difference between the splitting Ce^{3+} ^2e_g levels in the LCAMAS system will change with the shape of the dodecahedral site in which the Ce^{3+} ions are replaced because the coordination shape plays a critical role in both the centroid shift (ε_c) and crystal field splitting (ε_{cfs}) of the 5d manifold. The 5d ε_c for Ce^{3+} can be expressed by the following equation[26,27]

$$\varepsilon_c = 1.79 \times 10^{13} \sum_{i=1}^{N} \frac{\alpha_{sp}^i}{(R_i - 0.6\Delta R)^6} \tag{1}$$

where R_i is the distance between Ce^{3+} (in units of pm) and anion i in the undistorted lattice, and $0.6\Delta R$ is a correction for the relaxation of the lattice around Ce^{3+}. The summation is over all N anions that coordinate Ce^{3+}. α_{sp}^i is the spectroscopic polarizability of anion i in 10^{-30} m^3 or Å^3. For the oxides,[28]

$$\alpha_{sp}^O = 0.33 + \frac{4.8}{\chi_{av}^2} \tag{2}$$

where χ_{av} is the average electronegativity (χ) of the cations. In Table 1, the χ_{av} values increase as x increases. The χ_{av} of the cations at the {A} sites is decreased due to the substitution of Lu^{3+} ($\chi_{Lu} = 1.27$) with Ca^{2+} ($\chi_{ca} = 1.00$) and is also decreased at the [B] sites because the Al^{3+} ($\chi_{Al} = 1.61$) is substituted with Mg^{2+} ($\chi_{Mg} = 1.31$). The increase in the χ_{av} of the cations at the (C) sites is due to the substitution of Al^{3+} ($\chi_{Al} = 1.61$) with Si^{4+} ($\chi_{Si} = 1.90$). When calculating χ_{av}, the mole of the sites to be substituted is also considered so that the difference in χ is similar; the χ_{av} is increased in the LCAMAS system as a result. From eqs 1 and 2, we can expect that the centroid shift will decrease with the increase in χ_{av}, and this is in line with a previous report that the Ce^{3+} ε_c of LuAG and LCMS was estimated at approximately 14,300 and 13,300 cm^{-1}, respectively.[25] It is clear that a prediction about the changing trend of covalent character of Ce−O bonds from LuAG:Ce^{3+} ($x = 0$) to LCMS:Ce^{3+} ($x = 1$) can be made. The covalent character of the Ce−O bonds in garnets is affected by the cations at the {A}, [B], and (C) sites because the O^{2-} anion that is connected with Ce^{3+} is also shared by the other three cations, as mentioned before. Increasing the χ of the cations at the {A}, [B], and (C) sites may decrease the covalent character of the Ce−O bonds in Ce^{3+}-doped garnets. Moving the O^{2-} ions away from Ce^{3+} usually causes a decrease in ε_c, thus destabilizing the 5d levels because of the weaker orbital overlap between the Ce^{3+} and O^{2-}, which is commonly referred to as the nephelauxetic effect. Additionally, the expansion of the {A}O$_8$ dodecahedron caused by the partial replacement of the Lu^{3+} ions with Ca^{2+} ions should weaken the ε_{cfs} of the 5d levels, increasing the energy of the lowest ^2e_g level and causing a blue-shift. However, the results of the PL in Figure 2 show that the λ_{max} is red shifted with the decrease in ε_c and the increase in x of the LCAMAS:Ce^{3+} phosphors. Therefore, the ε_{cfs} of the Ce^{3+} in the LCAMAS system was investigated. The ε_{cfs} of the 5d levels can be expressed as[29]

$$\varepsilon_{cfs} = \beta_{poly}^Q R_{av}^{-2} \tag{3}$$

where β_{poly}^Q is a constant that depends on the type of the coordination polyhedron, Q is 3+ for Ce^{3+}, and R_{av} is close to the average distance between the anions and cations that are replaced by Ce^{3+}. R_{av} is defined as[29]

$$R_{av} = 1/N \sum_{i=1}^{N} (R_i - 0.6\Delta R) \tag{4}$$

where R_i (pm) are the bond lengths to the N coordinating anions in the unrelaxed lattice. $\Delta R = R_M - R_{Ln}$, where R_M is the ionic radius of the cation that is replaced by the lanthanide Ln with an ionic radius R_{Ln}. In this case, the R_{av} values were dominant in ε_{cfs} because the coordination polyhedron of Ce^{3+} was at the same site in the LCAMAS system. As mentioned

above, the average size of the dodecahedral site was slightly larger at $x = 1$ ($r_{av} = 2.39$ Å) than $x = 0$ ($r_{av} = 2.35$ Å) in these solid-solution samples. The replacement of the {A} site with a larger cation generally results in an increase in the tetragonal ε_{cfs} that can lead to red-shifting. Therefore, we assumed that the red-shift of the λ_{max} in the LCAMAS system may be predominantly attributed to the strong ε_{cfs} of the Ce^{3+} 5d manifold with an increasing x.

The ^2e_g energy of the Ce^{3+} ions in the garnet phosphor combined with a larger Stokes shift reduces the energy barrier required for nonradiative crossovers from the ^2e_g level to the $4f^1$ ground state, resulting in the stronger thermal quenching (TQ) of the Ce^{3+} ions, as depicted in Figure 2d. The temperature-dependent photoluminescence spectra for this solid-solution series was measured from the ambient temperature to 200 °C. Thermal stability is important for ensuring high efficiency in a phosphor-converted device. The trend in the TQ behavior decreased depending on the increase in x. The emission intensity of the LCMS:Ce^{3+} ($x = 1$) decreased faster than that of the parent LuAG:Ce^{3+} ($x = 0$) with increasing temperature. However, all three compositions showed good thermal stability (>80%@150 °C) and can therefore be applied to high-power lighting applications. To better understand the dependence of thermal stability on a structural change in the solid-solution ratio (x) of LuAG-LCMS, the band gaps (E_g) and the Debye temperatures (Θ_D) of the LCAMAS compositions are calculated as shown Table 2.

Table 2. Calculated Band Gap (E_g) and Debye Temperature (Θ_D) for Different Solid-Solution Ratios in LCAMAS:Ce^{3+}

| host composition	$E_g{}^a$ (eV)	Θ_D (K)
LuAG:Ce^{3+} ($x = 0$)	6.33	605
LCAMAS:Ce^{3+} ($x = 0.1$)	6.18	605
LCAMAS:Ce^{3+} ($x = 0.3$)	6.15	597
LCAMAS:Ce^{3+} ($x = 0.5$)	5.91	592
LCAMAS:Ce^{3+} ($x = 0.7$)	5.67	593
LCMS:Ce^{3+} ($x = 1$)	5.55	593

^{a}The band gap was calculated using screened hybrid Heyd−Scuseria−Ernzerhor functionals.

The host E_g may be used as a proxy in order to estimate the photoionization energy, and Θ_D can be used to estimate the rigidity of a crystal. With the increase in x, the decrease in E_g means that the photoionization barrier would be smaller, which can affect the optical properties of the $5d_{e1}$ level (Figure 2a). This result also indicates that the LCAMAS compositions have high values of Θ_D that decrease slightly with the increase in x. Thus, LCAMAS:Ce^{3+} phosphors have high thermal stability, and LCAMAS:Ce^{3+} ($x = 0.7$ and 1) phosphors have the lowest Θ_D (593 K), resulting in a comparatively weaker thermal stability.

3.2. Enhancement of Optical Property Using Cation-Size Mismatch. Information regarding the emission wavelengths and thermal quenching properties of the garnet solid-solution series that resulted from the structural changes caused by substitution was given in Section 3.1. Based on these results, it was found that the change to the dodecahedral site, which is substituted with an activator, has a significant effect on the optical properties by substituting three sites in the garnet structure. Investigation was also carried out concerning the variation in the thermal stability of the phosphor according to the formation of E_g and the calculated Θ_D of the host by the

solid solution. Therefore, cation-size mismatch, which is carried out via the substitution of Ba^{2+} ions into the dodecahedral and octahedral sites, is applied to increase the structural changes and observe the environment around the Ce^{3+} ions. Ba^{2+} ions were substituted in the {Ca^{2+}} and [Mg^{2+}] sites in the LCAMAS:Ce^{3+} ($x = 0.1$) system.

Figure 3 presents the Rietveld refinement results for S1 ($Lu_{2.8}Ba_{0.1}Ce_{0.1}Al_{2.8}Ba_{0.2}Al_{2.7}Si_{0.3}O_{12}$). The structural parame-
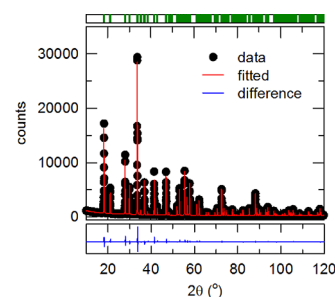
Figure 3. Rietveld refinement of $Lu_{2.9}Ba_{0.1}Al_{1.8}Ba_{0.2}Al_{2.7}Si_{0.3}O_{12}$:$Ce^{3+}$ (S1) using X-ray powder diffraction. Black circles represent the observed intensities, and the red solid lines indicate the calculated ones. A difference (obs.−cal.) plot is shown beneath.

ters determined by the Rietveld refinement of the powder XRD data are listed in Table 3. The refinement confirmed the single-phase nature of the compound in the cubic space group $Ia\overline{3}d$ (a = 11.91 Å and V = 1691.18 Å^3). From these results, it is apparent that a solid solution with garnet can form with specific Ba^{2+} substitutions in the structure of the garnet.

Figure 4 shows the excitation and emission spectra of LCAMAS:Ce^{3+} ($x = 0.1$) and S1, as compared with those of commercial LuAG:Ce^{3+} phosphor (intematix, GAL520). The spectroscopic properties of the solid-solution phosphors depending on the substituted ions for the ratio ($x = 0.1$) are given in Table 4. The PL emission wavelength was 513 nm in S1, which is blue shifted compared to those of LuAG:Ce^{3+} ($x = 0$) and LCAMAS:Ce^{3+} ($x = 0.1$). The value of fwhm was smaller than that of the mother samples. As discussed above, this trend comes from the differences in covalency in the environment around the Ce^{3+} ion. The χ_{av} of the cations at the {A} sites decreased due to the substitution of {Lu^{3+}/Ca^{2+}} with {Lu^{3+}/Ba^{2+}} ($\chi_{Ba} = 0.89$), and the χ_{av} of the cations at the [B] sites also decreased because of the substitution of [Mg^{2+}] with [Ba^{2+}]. Decreasing the χ_{av} led to an increase in the covalency of the Ce−O bonds and ε_c, leading to the blue-shifting of λ_{max} and the narrow fwhm with the Ba^{2+} ion substitutions. The emission intensity of S1 was approximately 109% higher than that of the commercial LuAG:Ce^{3+} phosphor, and it showed a high QY (93%), which is suitable for use in commercial solid-state lighting applications. The calculated E_g and Θ_D of S1 were decreased, indicating that the substitution of Ba^{2+} ions in the LCAMAS system can also affect the thermal stability.

To confirm that Ba^{2+} ions are present in the LCAMAS system, solid-state ^{27}Al NMR and XPS spectra (Ba 3d and Ce 3d) of the LCAMAS:Ce^{3+} ($x = 0.1$) and S1 were produced as presented in Figure 5. The corresponding solid-state ^{27}Al NMR spectra and normalized spectra were collected at 9.4 T (30 Hz), under magic-angle spinning (MAS) for LuAG:Ce^{3+} ($x = 0$), LCAMAS:Ce^{3+} ($x = 0.1$), and S1, as shown in Figure 5a,b, respectively. The ^{27}Al MAS spectra of all the samples exhibit a resonance peak at a chemical shift of 5 ppm

Table 3. Atomic Position and Site Occupancy Factor Obtained from the Rietveld Refinement of $Lu_{2.9}Ba_{0.1}Al_{1.8}Ba_{0.2}Al_{2.7}Si_{0.3}O_{12}$

		$Lu_{2.9}Ba_{0.1}Al_{1.8}Ba_{0.2}Al_{2.7}Si_{0.3}O_{12}$ [a]				
atom	symmetry multiplicity	x	y	z	$100 \times U_{iso}/\text{Å}^2$	occupancy
Lu	24c	1/8	0	1/4	0.014	0.9334
Ba	24c	1/8	0	1/4	0.014	0.0666
Al	16a	0	0	0	3.567	0.9
Ba	16a	0	0	0	3.567	0.1
Al	24d	3/8	0	1/4	0.277	0.9
Si	24d	3/8	0	1/4	0.277	0.1
O	96h	−0.03218	0.05235	0.15365	0.495	1.0

[a](R_{wp} = 7.62, χ^2 = 1.89).
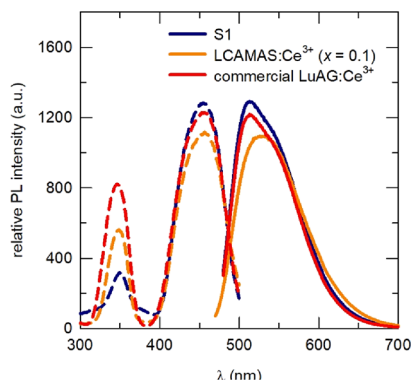
Figure 4. Photoluminescence excitation and emission spectra of $Lu_{2.9}Ca_{0.1}Al_{1.8}Mg_{0.2}Al_{2.7}Si_{0.3}O_{12}$:$Ce^{3+}$ (LCAMAS:Ce^{3+}, x = 0.1), $Lu_{2.9}Ba_{0.1}Al_{1.8}Ba_{0.2}Al_{2.7}Si_{0.3}O_{12}$:$Ce^{3+}$ (S1), and commercial LuAG:Ce^{3+} phosphors.

Figure 5. (a) Solid-state ^{27}Al MAS spectra and (b) normalized solid-state ^{27}Al MAS spectra for LuAG:Ce^{3+}, LCAMAS:Ce^{3+} (x = 0.1), and S1. Inserts of (a) and (b) show the shift in the peak position for AlO_6. (c) Ba 3d and (d) Ce 3d XPS spectra of $Lu_{2.9}Ca_{0.1}Al_{1.8}Mg_{0.2}Al_{2.7}Si_{0.3}O_{12}$:$Ce^{3+}$ (LCAMAS:Ce^{3+}, x = 0.1) and $Lu_{2.9}Ba_{0.1}Al_{1.8}Ba_{0.2}Al_{2.7}Si_{0.3}O_{12}$:$Ce^{3+}$ (S1). The solid and dashed lines are the fitting data of Ce^{3+} (pale orange) and Ce^{4+} (pale violet) 3d level, respectively.

corresponding to the $[Al^{3+}]O_6$ octahedral sites, together with two resonance peaks, where chemical shifts of 50 and 75 ppm occurred that were associated with the $(Al^{3+})O_4$ tetrahedral sites. Based on the spectra of LuAG:Ce^{3+} phosphor, the peaks of the LCAMAS:Ce^{3+} (x = 0.1) sample were shifted with an associated broadening of the spectra from the distortion of the Al−O coordination. The intensities of the peaks in S1 indicate that the number of ^{27}Al atoms was reduced. Figure 5c depicts the XPS spectra of Ba 3d of LCAMAS:Ce^{3+} (x = 0.1) and S1. The two peaks at 779.5 and 795.0 eV in the spectrum of Ba^{2+} 3d of S1 indicate the presence of the Ba^{2+} $3d_{5/2}$ and $3d_{3/2}$ levels, respectively. Figure S3 shows the XPS spectra of the other Ba^{2+} energy levels from which the Ba^{2+} ions can be observed more clearly. Figure 5d displays the Ce $3d_{5/2}$- and $3d_{3/2}$-level peaks, which are accompanied by satellite peaks, suggest the presence of traces of Ce^{4+} ions in the samples. The amount of Ce^{3+}, discerned from the ratio of Ce^{3+} to Ce^{4+} ions in the XPS results (Table S4), was higher in S1 than LCAMAS:Ce^{3+} (x = 0.1), which is supported by the relatively high PL intensity. The variations in TQ with different excitation energies that are related to the Ce^{3+} 5d levels were measured from the room temperature up to 200 °C (Figure 6).

LCAMAS:Ce^{3+} (x = 0.1) and S1 showed good thermal stability (>85%@150 °C) although the PL intensity decreased and the maximum emission wavelength of these phosphors was red shifted with increasing temperature. This phenomenon is a typical thermal quenching of the 5d−4f transition of Ce^{3+}, which is explained by the thermally activated crossover mechanism in the configuration coordinate diagram. The LCAMAS:Ce^{3+} (x = 0.1) phosphor exhibited stronger thermal stability at higher energy levels ($5d_{e1}$, λ_{ex} = 346 nm; $5d_{e2}$, λ_{ex} = 460 nm), and S1 showed the opposite behavior. As indicated

Table 4. Spectroscopic Properties of the Solid Solution Phosphor Depending on the Ratio (x), Recorded at Room temperature

phosphor	λ_{ex1} (nm)	λ_{ex2} (nm)	λ_{em} (nm)	fwhm (nm)	$\Delta\delta$ (cm^{-1})	Stokes shift (cm^{-1})	E_g (eV)	Θ_D (K)	QY (%)
LuAG:Ce^{3+} (x = 0)	349	456	526	97	6723.48	2918.41	6.33	605	96
LCAMAS:Ce^{3+} (x = 0.1)[a]	346	456	521	96	6971.91	2735.97	6.18	605	90
S1[b]	349	455	513	90	6675.27	2484.85	5.55	537	93
commercial LuAG:Ce^{3+}	349	455	513	91	6675.27	3484.85			98[27]

[a]$Lu_{2.9}Ca_{0.1}Al_{1.8}Mg_{0.2}Al_{2.7}Si_{0.3}O_{12}$:$Ce^{3+}$. [b]$Lu_{2.9}Ba_{0.1}Al_{1.8}Ba_{0.2}Al_{2.7}Si_{0.3}O_{12}$:$Ce^{3+}$.
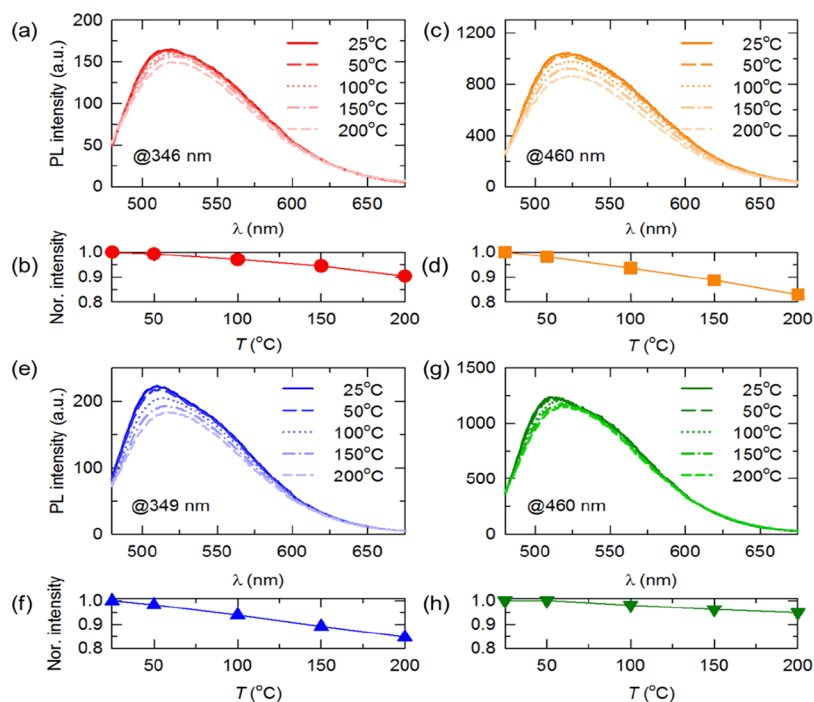
Figure 6. Temperature dependence of emission spectra of $Lu_{2.9}Ca_{0.1}Al_{1.8}Mg_{0.2}Al_{2.7}Si_{0.3}O_{12}:Ce^{3+}$ (LCAMAS:Ce^{3+}, $x = 0.1$) under (a) $\lambda_{ex} = 346$ nm and (c) $\lambda_{ex} = 450$ nm, as recorded over the temperature range 25−200 °C. Normalized intensity [(b) $\lambda_{ex} = 346$ nm and (d) $\lambda_{ex} = 450$ nm] vs temperature for LCAMAS:Ce^{3+} ($x = 0.1$). Temperature dependence of emission spectra of $Lu_{2.9}Ba_{0.1}Al_{1.8}Ba_{0.2}Al_{2.7}Si_{0.3}O_{12}:Ce^{3+}$ (S1) under (a) $\lambda_{ex} = 349$ nm and (c) $\lambda_{ex} = 450$ nm, as recorded over the temperature range 25−200 °C. Normalized intensity [(b) $\lambda_{ex} = 349$ nm and (d) $\lambda_{ex} = 450$ nm] vs temperature for S1.
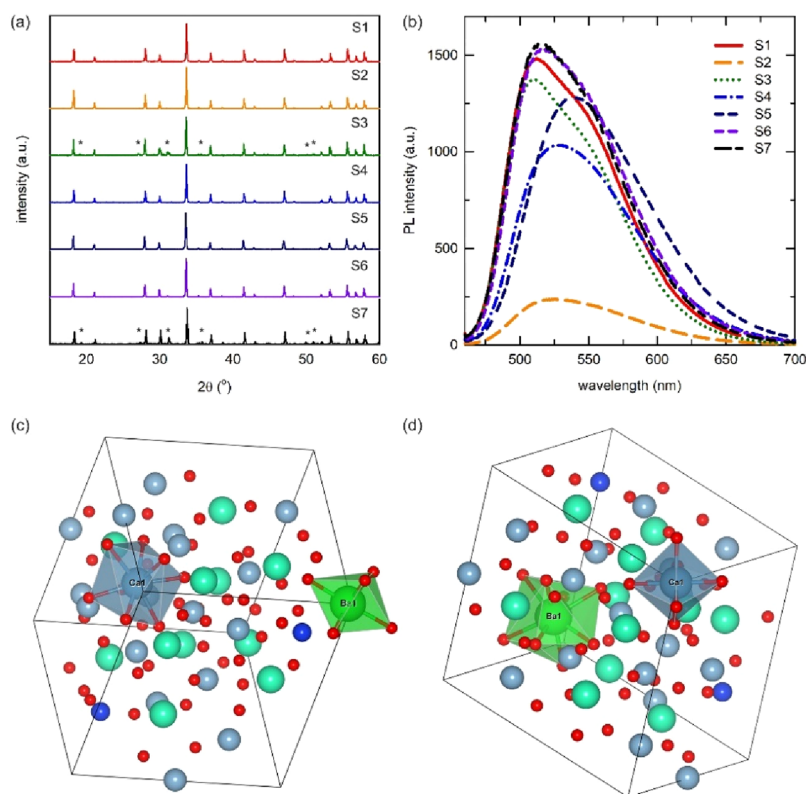
Figure 7. (a) XRD patterns and (b) photoluminescence emission spectra of S1−7 under excitation at 450 nm. The star marks in (a) indicate the peaks of the unknown impurity phase. (c,d) Models for the calculation of total energy and site energy for the substitution of (c) Ba and (d) Ca ions in the octahedral site of S6. Lu in dodecahedral site is light blue. Al in octahedral and tetrahedral sites is mint. Si in tetrahedral site is blue. O is red.

Table 5. Details of the Composition and Calculated Distributions of Cation-Size Variance σ^2 for S1−7

sample	composition	σ^2 {A} site	[B] site	(C) site	average
S1	$Lu_{2.8}Ba_{0.1}Ce_{0.1}Al_{1.8}Ba_{0.2}Al_{2.7}Si_{0.3}O_{12}$	0.0070	0.0598	0.0015	0.0182
S2	$Lu_{2.8}Ba_{0.1}Ce_{0.1}Al_{1.8}Mg_{0.2}Al_{2.7}Si_{0.3}O_{12}$	0.0070	0.0031	0.0015	0.0040
S3	$Lu_{2.6}Ba_{0.3}Ce_{0.1}Al_{1.4}Ba_{0.6}Al_{2.1}Si_{0.9}O_{12}$	0.0181	0.1395	0.0035	0.0430
S4	$Lu_{2.6}Ba_{0.3}Ce_{0.1}Al_{1.8}Mg_{0.2}Al_{2.7}Si_{0.3}O_{12}$	0.0181	0.0031	0.0015	0.0081
S5	$Lu_{2.6}Ba_{0.3}Ce_{0.1}Al_{1.4}Mg_{0.6}Al_{2.1}Si_{0.9}O_{12}$	0.0181	0.0072	0.0035	0.0099
S6	$Lu_{2.8}Ca_{0.1}Ce_{0.1}Al_{1.8}Ba_{0.2}Al_{2.7}Si_{0.3}O_{12}$	0.0015	0.0598	0.0015	0.0161
S7	$Lu_{2.6}Ca_{0.3}Ce_{0.1}Al_{1.4}Ba_{0.6}Al_{2.1}Si_{0.9}O_{12}$	0.0026	0.1395	0.0035	0.0372

previously, the E_g and Θ_D calculated for S1 could be assigned to the weaker thermal stability. The differences in the thermal stability at higher energy levels might be related to photo-ionization that is connected to the conduction band of the structure from calculation data.[4,30] A decrease in the intensity of the $5d_{e1}$ level caused by the substitution of Ba^{2+} ions was observed in the LCAMAS system in Figure 4, indicating that large Ba^{2+} ions are substituted in the LCAMAS system, which results in a smaller value of E_g, indicating that photoionization can occur more easily as the Ce^{3+} $5d_{e1}$ level approaches the conduction band. However, TQ exhibited a drastic improvement in thermal stability (95%@150 °C) at lower energy levels ($5d_{e2}$). This improvement could be related to the smaller Stokes shift than that occurring in the mother samples. A short Stokes shift indicates that there is a short energy path leading to a non-radiative transition, which may be associated with an improved thermal quenching property.

Figure S4 shows the schematic energy-level diagram for Ce^{3+} in the LCAMAS samples and illustrates the E_g discussed above. An increase in the crystal field strength from the change of the dodecahedral site due to an increased x in the solid solution of LCAMAS:Ce^{3+} phosphors ultimately leads to the red-shift in the emission peak. In contrast, the replacement of Ba^{2+} ions into the {Ca^{2+}} and [Mg^{2+}] sites also leads to a decrease in the strength of the crystal field, which can lead to the emission of blue shifted light compared to that of pristine garnet. However, the effect of substituting Ba^{2+} ions into the LCAMAS:Ce^{3+} phosphor remains to be understood.

Therefore, we investigated the change of optical properties in the LCAMAS phosphors *via* cation-size mismatch, which included increasing the amount of Ba^{2+} ions in the dodecahedral and octahedral sites in order to investigate the changes in optical properties. Figure 7a shows the XRD patterns of samples according to the amount of Ba in the sample. Details of the composition of the samples were described in the Experimental Section. S1, S2, S4, and S6 all started from an LCAMAS:Ce^{3+} ($x = 0.1$) composition, and S3, S5, and S7 were controlled starting from an LCAMAS:Ce^{3+} ($x = 0.3$) composition, in which Ba^{2+} ions were substituted into different sites in order to observe the effects of the Ba^{2+} ions in a LCAMAS solid-solution system. Most samples showed a single phase except for S3 and S7. Impurities were found in S3 and S7, where the amount of Ba (mol %) was relatively higher than that in the other samples, and high σ^2 values were also observed in these samples, as described in Table 4. The calculated σ^2 values showed a larger change in the octahedral site than the dodecahedral site, which is considered to be an effect of the larger size of the Ba^{2+} ion compared to the size of the mother garnet structure. The impurity phase in the XRD results was observed only when the σ^2 value exceeded 0.02. From this result, it can be stated that there is a limit to the

value of cation-size mismatch for replacing the original ions in the structure. Figure 7b displays the PL emission spectra of S1−7. The λ_{em} and fwhm of S1−7 with LCAMAS:Ce^{3+} ($x = 0.1$ and 0.3) are summarized in Table 5.

Based on S1, the change in λ_{em} and the emission intensity due to Ba substitution can be split into three parts. (**1**) **Ba^{2+} ions substitution in the dodecahedral site only**: The samples in which Ba^{2+} ions were substituted only into the dodecahedral site (S2, S4, and S5) showed a red-shift in the λ_{em} and a broadening of the fwhm. Comparing S2 and S4, in which the concentration of Ba^{2+} ions in the dodecahedral site was increased with octahedral and tetrahedral sites fixed, the λ_{em} of the samples was almost the same, but the intensity of the PL was greatly increased. S5, which was started from LCA-MAS:Ce^{3+} ($x = 0.3$), produced a red-shift in λ_{em} that was slightly different with a wide fwhm compared with LCAMAS:Ce^{3+} ($x = 0.3$). The PL intensity of S5 was also significantly higher than that of S2, which was started from LCAMAS:Ce^{3+} ($x = 0.1$). This tendency of the PL intensity is contrary to the replacement of Ca in the dodecahedral site by the solid solution discussed in Section 3.1. Additionally, S5 showed a larger Stokes shift (Figure S6). (**2**) **The substitution of Ba^{2+} ions in the octahedral site only**: The samples in which Ba^{2+} ions were placed into the octahedral site (S3, S6, and S7) showed a blue-shift in λ_{em} and a narrow fwhm Thus, sample S7, in which there was an increase in the Ba concentration in the LCAMAS:Ce^{3+} phosphors, showed more blue-shift in λ_{em} and a narrow fwhm compared with S6. S6 and S7 showed 107% higher PL intensity than S1. (**3**) **Ba^{2+} ions are substituted in both the dodecahedral and octahedral sites**: Sample S3, which has a higher concentration of Ba^{2+} ions than S1, showed a slight blue-shift of λ_{em} and a narrow fwhm with a low PL intensity.

From these results, we can predict the effects of Ba^{2+} ions by replacement in the dodecahedral and octahedral sites of S1. Basically, the 2θ degree in the XRD result is changed by the solid solution. If the Ba^{2+} ions are sufficiently replaced in a composition, the 2θ value will be shifted by a small angle. When comparing samples that started substitution with LCAMAS:Ce^{3+} ($x = 0.1$), the value of 2θ varies according to the substitution site, as seen in Figure S5a. The 2θ value of (420) as the main peak in the XRD of S6 (substitution in the octahedral site) is 33.60°, which is slightly smaller than that of S2 (33.64°, substitution in the dodecahedral site) and S1 (33.68°, substitutions in both sites). A comparison of S2 and S4 clearly shows where the Ba^{2+} ions are substituted. S2 and S4 have exactly the same amount of Ba in mols; however, in S4, substitution has taken place only in the dodecahedral site. The 2θ values are almost the same as predicted by Figure S5b. This result suggests that Ba^{2+} ions prefer to be substituted into the dodecahedral site. To understand this effect, the total energy

and site energy of S6 were calculated as in Table 6. Figure 7c,d show the models in which the Ba^{2+} ions are substituted into

Table 6. Maximum Emission Wavelength (λ_{em}) full-width-at-half-maximum (fwhm) From PL Emission Spectra of LCAMAS:Ce^{3+} (x = 0.1 and 0.3) and S1−7

sample	λ_{em} (nm)	fhwm (nm)
LCAMAS:Ce^{3+} (x = 0.1)	521	96
LCAMAS:Ce^{3+} (x = 0.3)	532	98
S1	512	90
S2	528	97
S3	510	88
S4	527	99
S5	538	100
S6	518	93
S7	514	90

the dodecahedral and octahedral sites, respectively. The site energy of Ba^{2+} ions in the octahedral site with Ca ions in the dodecahedral site was higher than the case in which Ba^{2+} ions were substituted into the dodecahedral site (Table 7). This

Table 7. Total Energy and Site Energy from the Substitution of Ba and Ca Ions in the Octahedral Site of S6

sample	total energy (eV)	site energy (eV)
$Lu_{2.75}Ca_{0.25}Al_{1.75}Ba_{0.25}Al_{2.5}Si_{0.5}O_{12}$	−623.45	1.54
$Lu_{2.75}Ba_{0.25}Al_{1.75}Ca_{0.25}Al_{2.5}Si_{0.5}O_{12}$	−624.99	0

means that the Ba^{2+} ions are more stable in the dodecahedral site than the octahedral site. If a Ca^{2+} ion is substituted into the octahedral site, it is consistent with the previous tendency that if the octahedral site is replaced with a smaller ion (Ba → Ca), λ_{em} is red shifted and the fwhm is wider compared with S1 and S3. Evidence that the Ba^{2+} ions are stably replaced in the dodecahedral site is also shown by comparing the PL intensities of S2, S4, and S5. The PL intensity was found to increase as the amount of molar Ba was increased in the composition and the solid-solution ratio (S2 < S4 < S5); the fwhm of the PL emission spectra exhibited a similar trend. In S5, in which Ba was substituted into the LCAMAS:Ce^{3+} (x = 0.3) instead of Ca, a red-shift was observed with a broadening fwhm compared with the pristine Ca-doped sample (Table 5). This behavior is the opposite of the expected blue-shift because of the larger size of the Ba^{2+} ions. These results might be expected to affect the ε_{cfs} of the Ce^{3+} ions when larger Ba^{2+} ions are substituted in the dodecahedral sites, further increasing the distortion of the site as the ε_{cfs} of Ce^{3+} is suppressed.[31] When the solid-solution ratio was increased, the interaction among the increased $[Mg^{2+}]$-(Si^{4+}) ions and $\{Ba^{2+}\}$, which is able to effect the ε_{cfs} of the Ce^{3+} ions, moved to a longer wavelength and the intensity of the PL emission appeared to increase together with an increase in the Stokes shift (Figure S6). This observation also suggests that the inhomogeneous broadening of the Ce^{3+} emission acts as an outcome of the random distribution of the Lu^{3+}/Ba^{2+} sites in the different unit cells of the LCAMAS:Ce^{3+} system.[32]

Although Ba^{2+} ions were preferentially substituted in the dodecahedral sites of the garnet structure, changes in the optical properties were observed even when substitution took place at the octahedral site. These phenomena were deduced from the NMR results in Figure 5a. The normalized solid-state

^{27}Al NMR spectra are described in Figure 5b for better understanding. There are different sidebands in the Ba-doped sample (S1) and the Ba-undoped samples (LuAG:Ce^{3+} and LCAMAS:Ce^{3+}, x = 0.1). It is well known that spinning sidebands originate from dipolar interactions between the nuclear spin and the unpaired electron spins of paramagnetic ions;[33,34] this occurred between the ^{27}Al spin and the unpaired electron spins of Ce^{3+} ions in this system. From this result, we can assume that the LuAG:Ce^{3+} and the LCAMAS:Ce^{3+} (x = 0.1) have similar environments around the AlO_4 tetrahedral and the AlO_6 octahedral sites; however, S1 has a different environment. This may be because the spinning sidebands in the NMR spectra of S1 support the fact that the Ba^{2+} ions are occupied with a pseudo-covalent bond character in the interstitial sites of the LCAMAS:Ce^{3+} (x = 0.1) phosphor.[35] Thus, the inset of Figure 5b shows that the NMR spectra originated from AlO_6 and the fwhm of samples was changed. S1 has a narrower fwhm (3.34 ppm) than LuAG:Ce^{3+} (4.03 ppm), which was narrower than LCAMAS:Ce^{3+} (x = 0.1) (5.18 ppm). It is possible that the presence of $[Mg^{2+}]$ and (Si^{4+}) in the LCAMAS:Ce^{3+} (x = 0.1) samples was due to the increase in disorder around the AlO_6 octahedral, which resulted from the presence of unpaired electrons from the Ce^{3+} ions.[36,37] On the other hand, $[Ba^{2+}]$ with (Si^{4+}) in S1 decrease in disorder around the AlO_6 octahedral. The dodecahedral, octahedral, and tetrahedral sites in the garnet structure are linked by oxygen ions as mentioned in Section 3.1, and there are structurally empty spaces.[38,39] Therefore, the Ba^{2+} ions that were replacements in the octahedral site might be substituted into the interstitial sites in the garnet structure, and the Ba^{2+} ions that remain beyond the substitution limit appear to produce impurity phases (S3 and S7). This substitution limit was assumed from the recalculation of the σ^2 values for the S6 and S7 samples, in which the Ba^{2+} ions are thought to have been substituted into the dodecahedral sites (Table S5). There are reduced values of σ^2 due to the size difference, but S7 still has a high value exceeding 0.02, which is predictable for the formation of an impurity phase.

4. CONCLUSIONS

In this study, we investigated the crystal chemistry and Ce^{3+} luminescence properties of LuAG:Ce^{3+} and LCMS:Ce^{3+} solid-solution garnets. There is strong evidence of a continuous solid solution between the previously reported LuAG:Ce^{3+} green and LCMSO:Ce^{3+} orange phosphor. Correspondingly, $\{Ca^{2+}\}$-$[Mg^{2+}]$-(Si^{4+}) substitutions in these solid-solution garnets are thought to be at the dodecahedral, octahedral, and tetrahedral sites, respectively. The composition regions for phase stability have been described and explained using known crystal chemistry trends within the garnet family. We have also demonstrated that as the composition moves through this solid solution, the Ce^{3+} emission continuously shifts, allowing for the flexibility of the color in different solid-state lamp applications. The emission of the as-prepared $Lu_{2.8}Ca_{0.1}Ce_{0.1}Al_{1.8}Ba_{0.2}Al_{2.7}Si_{0.3}O_{12}$ phosphor under λ_{ex} = 450 nm was measured at 116%, compared with the commercial LuAG:Ce^{3+} phosphor. An initial explanation for the significant blue-shift in the emission band of Ce^{3+} in this garnet compared to LuAG:Ce^{3+} was also presented, along with the high quantum efficiency of this material and the reduction in the absorption of this phosphor in the green spectral region. Furthermore, to confirm the sites where the Ba^{2+} ions are replaced, Ba^{2+} ions were substituted at up to 10 mol % of the

dodecahedral sites and octahedral sites in the compositions, respectively. In conclusion, the Ba^{2+} ions preferred the dodecahedral site, but small amounts were observed at the octahedral site, thereby affecting the Ce^{3+} emissions. This was confirmed by the NMR analysis and computational calculations. On the basis of these results, the new green garnet phosphor developed *via* the cation-size mismatch could potentially be applied in high-power LEDs and laser diodes.

■ ASSOCIATED CONTENT

Ⓢ Supporting Information

The Supporting Information is available free of charge at https://pubs.acs.org/doi/10.1021/acs.chemmater.0c00095.

Information on the lattice parameter and crystallographic details of LCAMAS; optical analysis (maximum wavelength of emission, fwhm, and quantum yield) of LCAMAS:Ce^{3+} phosphors; deconvolution data of Ce 3d XPS of LCAMAS:Ce^{3+} ($x = 0.1$) and S1; calculation of σ^2 of S6 and S7; structure of LuAG and LCMS; Rietveld refinement of LCAMAS:Ce^{3+} phosphors; XPS of S1 and LCAMAS:Ce^{3+} ($x = 0.1$); schematic diagram of LCAMAS:Ce^{3+} phosphors; XRD of S1, S2, and S6; and normalized PL spectra of S1−7 (PDF)

■ AUTHOR INFORMATION

Corresponding Authors

Zhenbin Wang − *Department of NanoEngineering, University of California, San Diego, La Jolla, California 92093, USA;* Email: zwang@fysik.dtu.dk

Won Bin Im − *Division of Materials Science and Engineering, Hanyang University, Seoul 04763, Republic of Korea;* ⓞ orcid.org/0000-0003-2473-4714; Email: imwonbin@hanyang.ac.kr

Authors

Yoon Hwa Kim − *Wearable Platform Materials Technology Center, Korea Advanced Institute of Science and Technology (KAIST), Daejeon 34141, Republic of Korea*

Ha Jun Kim − *Division of Materials Science and Engineering, Hanyang University, Seoul 04763, Republic of Korea*

Shyue Ping Ong − *Department of NanoEngineering, University of California, San Diego, La Jolla, California 92093, USA;* ⓞ orcid.org/0000-0001-5726-2587

Complete contact information is available at:
https://pubs.acs.org/10.1021/acs.chemmater.0c00095

Author Contributions

[⊥]Y.H.K. and H.J.K. contributed equally.

Notes

The authors declare no competing financial interest.

■ ACKNOWLEDGMENTS

■ REFERENCES

(1) Nakatsuka, A.; Yoshiasa, A.; Yamanaka, T. Cation distribution and crystal chemistry of $Y_3Al_{5-x}Ga_xO_{12}$ ($0 \leq x \leq 5$) garnet solid solutions. *Acta Crystallogr., Sect. B: Struct. Sci.* **1999**, *55*, 266−272.

(2) Xia, Z.; Meijerink, A. Ce^{3+}-Doped garnet phosphors: composition modification, luminescence properties and applications. *Chem. Soc. Rev.* **2017**, *46*, 275−299.

(3) Shao, Q.; Dong, Y.; Jiang, J.; Liang, C.; He, J. Temperature-dependent photoluminescence properties of $(Y, Lu)_3Al_5O_{12}$:Ce^{3+} phosphors for white LEDs applications. *J. Lumin.* **2011**, *131*, 1013−1015.

(4) Ueda, J.; Tanabe, S.; Nakanishi, T. Analysis of Ce^{3+} luminescence quenching in solid solutions between $Y_3Al_5O_{12}$ and $Y_3Ga_5O_{12}$ by temperature dependence of photoconductivity measurement. *J. Appl. Phys.* **2011**, *110*, 053102.

(5) Ueda, J.; Aishima, K.; Tanabe, S. Temperature and compositional dependence of optical and optoelectronic properties in Ce^{3+}-doped $Y_3Sc_2Al_{3-x}Ga_xO_{12}$ (x=0, 1, 2, 3). *Opt. Mater.* **2013**, *35*, 1952−1957.

(6) Shang, M.; Fan, J.; Lian, H.; Zhang, Y.; Geng, D.; Lin, J. A Double Substitution of Mg^{2+}−Si^{4+}/Ge^{4+} for $Al_{(1)}{}^{3+}$−$Al_{(2)}{}^{3+}$ in Ce^{3+}-Doped Garnet Phosphor for White LEDs. *Inorg. Chem.* **2014**, *53*, 7748−7755.

(7) Ji, H.; Wang, L.; Molokeev, M. S.; Hirosaki, N.; Xie, R.; Huang, Z.; Xia, Z.; ten Kate, O. M.; Liu, L.; Atuchin, V. V. Structure evolution and photoluminescence of $Lu_3(Al,Mg)_2(Al,Si)_3O_{12}$:$Ce^{3+}$ phosphors: new yellow-color converters for blue LED-driven solid state lighting. *J. Mater. Chem. C* **2016**, *4*, 6855−6863.

(8) Chen, Y.-B.; Tang, Z.-B.; Xu, X.-S.; Feng, D.-H.; Wang, Z.-Z.; Liu, Z.-Q. Tunable photoluminescence in $Lu_3Al_5O_{12}$−$Lu_2CaMg_2Si_3O_{12}$ solid solution phosphors manipulated by synchronous ions co-substitution. *RSC Adv.* **2016**, *6*, 43916−43923.

(9) Kishore, M. S.; Kumar, N. P.; Chandran, R. G.; Setlur, A. A. Solid Solution Formation and Ce^{3+} Luminescence in Silicate Garnets. *electrochem. Solid-State Lett.* **2010**, *13*, J77−J80.

(10) Kim, Y. H.; Kim, B. Y.; Viswanath, N. S. M.; Arunkumar, P.; Im, W. B. Structural and Optical Properties of Yellow-Emitting $CaGd_3ZrSc(AlO_4)_3$:Ce^{3+} Phosphor for Solid-State Lighting. *J. Korean Ceram. Soc* **2017**, *54*, 422−428.

(11) Hwang, H. Y.; Cheong, S.-W.; Radaelli, P. G.; Marezio, M.; Batlogg, B. Lattice Effects on the Magnetoresistance in Doped $LaMnO_3$. *Phys. Rev. Lett.* **1995**, *75*, 914−917.

(12) Rodriguez-Martinez, L. M.; Attfield, J. P. Cation disorder and size effects in magnetoresistive manganese oxide perovskites. *Phys. Rev. B: Condens. Matter Mater. Phys.* **1996**, *54*, R15622−R15625.

(13) Attfield, J. P. 'A' cation control of perovskite properties. *Cryst. Eng.* **2002**, *5*, 427−438.

(14) Chen, W.-T.; Sheu, H.-S.; Liu, R.-S.; Attfield, J. P. Cation-Size-Mismatch Tuning of Photoluminescence in Oxynitride Phosphors. *J. Am. Chem. Soc.* **2012**, *134*, 8022−8025.

(15) Lin, C. C.; Tsai, Y.-T.; Johnston, H. E.; Fang, M.-H.; Yu, F.; Zhou, W.; Whitfield, P.; Li, Y.; Wang, J.; Liu, R.-S.; Attfield, J. P. Enhanced Photoluminescence Emission and Thermal Stability from Introduced Cation Disorder in Phosphors. *J. Am. Chem. Soc.* **2017**, *139*, 11766−11770.

(16) Momma, K.; Izumi, F. VESTA 3 for three-dimensional visualization of crystal, volumetric and morphology data. *J. Appl. Crystallogr.* **2011**, *44*, 1272−1276.

(17) Kresse, G.; Furthmüller, J. Efficient iterative schemes for ab initio total-energy calculations using a plane-wave basis set. *Phys. Rev. B: Condens. Matter Mater. Phys.* **1996**, *54*, 11169−11186.

(18) Blöchl, P. E. Projector augmented-wave method. *Phys. Rev. B: Condens. Matter Mater. Phys.* **1994**, *50*, 17953−17979.

(19) Ong, S. P.; Richards, W. D.; Jain, A.; Hautier, G.; Kocher, M.; Cholia, S.; Gunter, D.; Chevrier, V. L.; Persson, K. A.; Ceder, G. Python Materials Genomics (pymatgen): A robust, open-source

python library for materials analysis. *Comput. Mater. Sci.* **2013**, *68*, 314−319.

(20) Heyd, J.; Scuseria, G. E.; Ernzerhof, M. Hybrid functionals based on a screened Coulomb potential. *J. Chem. Phys.* **2003**, *118*, 8207−8215.

(21) Heyd, J.; Scuseria, G. E.; Ernzerhof, M. Erratum: "Hybrid functionals based on a screened Coulomb potential" [*J. Chem. Phys.* 118, 8207 (2003)]. *J. Chem. Phys.* **2006**, *124*, 219906.

(22) Wang, Z.; Chu, I.-H.; Zhou, F.; Ong, S. P. Electronic Structure Descriptor for the Discovery of Narrow-Band Red-Emitting Phosphors. *Chem. Mater.* **2016**, *28*, 4024−4031.

(23) Ha, J.; Wang, Z.; Novitskaya, E.; Hirata, G. A.; Graeve, O. A.; Ong, S. P.; McKittrick, J. An integrated first principles and experimental investigation of the relationship between structural rigidity and quantum efficiency in phosphors for solid state lighting. *J. Lumin.* **2016**, *179*, 297−305.

(24) Shannon, R. D. Revised effective ionic radii and systematic studies of interatomic distances in halides and chalcogenides. *Acta Crystallogr., Sect. A: Cryst. Phys., Diffr., Theor. Gen. Crystallogr.* **1976**, *32*, 751−767.

(25) Setlur, A. A.; Heward, W. J.; Gao, Y.; Srivastava, A. M.; Chandran, R. G.; Shankar, M. V. Crystal Chemistry and Luminescence of Ce^{3+}-Doped $Lu_2CaMg_2(Si,Ge)_3O_{12}$ and Its Use in LED Based Lighting. *Chem. Mater.* **2006**, *18*, 3314−3322.

(26) Dorenbos, P. 5d-level energies of Ce^{3+} and the crystalline environment. III. Oxides containing ionic complexes. *Phys. Rev. B: Condens. Matter Mater. Phys.* **2001**, *64*, 125117.

(27) Dorenbos, P. Relating the energy of the $[Xe]5d^1$ configuration of Ce^{3+} in inorganic compounds with anion polarizability and cation electronegativity. *Phys. Rev. B: Condens. Matter Mater. Phys.* **2002**, *65*, 235110.

(28) Dorenbos, P. Calculation of the energy of the 5d barycenter of $La_3F_3[Si_3O_9]:Ce^{3+}$. *J. Lumin.* **2003**, *105*, 117−119.

(29) Dorenbos, P. A Review on How Lanthanide Impurity Levels Change with Chemistry and Structure of Inorganic Compounds. *ECS J. Solid State Sci. Technol.* **2013**, *2*, R3001−R3011.

(30) Lin, Y.-C.; Bettinelli, M.; Karlsson, M. Unraveling the Mechanisms of Thermal Quenching of Luminescence in Ce^{3+}-Doped Garnet Phosphors. *Chem. Mater.* **2019**, *31*, 3851−3862.

(31) Bachmann, V.; Ronda, C.; Oeckler, O.; Schnick, W.; Meijerink, A. Color Point Tuning for $(Sr,Ca,Ba)Si_2O_2N_2:Eu^{2+}$ for White Light LEDs. *Chem. Mater.* **2009**, *21*, 316−325.

(32) Kodama, N.; Yamaga, M.; Henderson, B. Inhomogeneous broadening of the Ce^{3+} luminescence in $CaYAlO_4$. *J. Phys.: Condens. Matter* **1996**, *8*, 3505−3512.

(33) Zagorodniy, Y.; Chlan, V.; Štěpánková, H.; Fomichov, Y.; Pejchal, J.; Laguta, V.; Nikl, M., Aluminum and Gallium Distribution in the $Lu_3(Al_{5-x}Ga_x)O_{12}$:Ce Multicomponent Garnet Scintillators Investigated by the Solid-State NMR and DFT calculations. In arXiv e-prints, **2018**.

(34) Herzfeld, J.; Berger, A. E. Sideband intensities in NMR spectra of samples spinning at the magic angle. *J. Chem. Phys.* **1980**, *73*, 6021−6030.

(35) Kim, D.; Jin, Y.-H.; Jeon, K.-W.; Kim, S.; Kim, S.-J.; Han, O. H.; Seo, D.-K.; Park, J.-C. Blue-silica by Eu^{2+}-activator occupied in interstitial sites. *RSC Adv.* **2015**, *5*, 74790−74801.

(36) Charpentier, T.; Martel, L.; Mir, A. H.; Somers, J.; Jégou, C.; Peuget, S. Self-healing capacity of nuclear glass observed by NMR spectroscopy. *Sci. Rep.* **2016**, *6*, 25499.

(37) Liu, T.-C.; Kominami, H.; Greer, H. F.; Zhou, W.; Nakanishi, Y.; Liu, R.-S. Blue Emission by Interstitial Site Occupation of Ce^{3+} in AlN. *Chem. Mater.* **2012**, *24*, 3486−3492.

(38) Stanek, C. R.; McClellan, K. J.; Levy, M. R.; Grimes, R. W. Extrinsic defect structure of $RE_3Al_5O_{12}$ garnets. *Phys. Status Solidi B* **2006**, *243*, R75−R77.

(39) Chiba, Y.; Yosida, T.; Date, M. Paramagnetic Resonance of Co^{2+} Ion in Yttrium Aluminum Garnet. *J. Phys. Soc. Jpn.* **1981**, *50*, 3925−3931.